buildings

MDPI

Article

Coupled Effects of Fines Content and Particle Shape on the Maximum Shear Modulus of Gap-Graded Soils: A DEM Investigation

Yuyang Tian, Xuan Wang *, Xingyang Liu and Xingxing Ai

College of Hydraulic Science and Engineering, Yangzhou University, Yangzhou 225009, China; 233201228@stu.yzu.edu.cn (Y.T.); 007975@yzu.edu.cn (X.L.); aixingxing2000@163.com (X.A.)
* Correspondence: wangx@yzu.edu.cn

Abstract

The maximum shear modulus (G_{max}) of soils is a critical parameter in geotechnical design and advanced constitutive modeling. While the effects of fines content (*FC*) and particle shape on G_{max} have been studied extensively, their collective influence on gap-graded soils remains poorly understood. This study employs the discrete element method (DEM) to systematically investigate the combined effects of fines content and particle shape on G_{max}, while strictly controlling all other variables. Numerical simulations were conducted on single-sized and binary mixtures with varying fines content of 0, 10%, and 20%, using five distinct particle shapes (with regularity indices ranging from 0.65 to 1.00) under different void ratios and confining pressures. The results show that G_{max} decreases with increasing *FC* but increases with greater particle irregularity. A coupled effect between *FC* and particle shape is observed, wherein the influence of particle shape becomes more pronounced at higher fines content. Micromechanical analysis indicates that the mechanical void ratio (e_m) effectively normalizes the effect of *FC* on G_{max} but does not fully account for the influence of particle shape due to variations in the proportion of inactive particles. Based on the Hardin model, empirical prediction equations for G_{max} are proposed by incorporating both *FC* and particle shape indices. The comparison between two-dimensional (2D) and three-dimensional (3D) shape descriptors demonstrates that the 3D regularity index provides a more accurate characterization of particle shape, leading to an increase in the coefficient of determination (R^2) from 0.90 to 0.94 and thereby improving predictive performance. This study highlights the importance of particle characteristics and the need for 3D shape parameters for reliable stiffness predictions in gap-graded granular materials.

Keywords: maximum shear modulus; fines content; particle shape; discrete element method; prediction model of G_{max}

Check for updates

Academic Editors: Bartolomeo Pantò and Antonio Caggiano

Received: 8 April 2026
Revised: 1 June 2026
Accepted: 24 June 2026
Published: 28 June 2026

Copyright: © 2026 by the authors. Licensee MDPI, Basel, Switzerland. This article is an open access article distributed under the terms and conditions of the Creative Commons Attribution (CC BY) license.

1. Introduction

Geotechnical engineering relies heavily on the accurate prediction of soil stiffness and strength for the safe and efficient design of civil infrastructure. For deformation analysis, the shear modulus across a range of shear strains is fundamental to characterizing both the elastic and nonlinear behavior of soils [1]. The rational selection of stiffness parameters is of critical importance for the numerical analysis of foundations, roadbeds, and slopes [2]. The shear modulus at very small shear strains (typically less than 0.0001%) is defined as the maximum shear modulus (G_{max}). G_{max} is a key input parameter in advanced

constitutive models, such as the Hardening Soil Small Strain (HSS) model, and is extensively used in finite-element analyses [3–5]. Experimental investigations into G_{max} are primarily conducted using bender element tests and resonant column tests [6,7]. These studies have revealed that several factors influence G_{max}, including void ratio (e) [8], mean effective stress (p') [9], degree of saturation [10], anisotropy [11], and particle characteristics (e.g., particle shape and size distribution) [12,13]. Among these, void ratio and mean effective stress have been identified as the most dominant. Accordingly, Hardin and Black [14] proposed an empirical model in the form of Equation (1) to estimate the G_{max} as a function of e and p':

$$G_{max} = Af(e)\left(\frac{p'}{p_a}\right)^n \quad (1)$$

where A is the material constant that depends on soil type, p_a is the reference atmospheric pressure for normalization purposes, n is the stress exponent, and $f(e)$ is the function of the void ratio, commonly found as in Equation (2) [14] and Equation (3) [15]:

$$f(e) = \frac{(x-e)^2}{1+e} \quad (2)$$

$$f(e) = e^c \quad (3)$$

where x and c are fitting parameters.

Recently, there has been growing interest in studying the mechanical behavior of gap-graded soils, as mixed granular materials generally appear in natural deposits rather than uniform soils. Gap-graded soils, such as sandy gravels or silty sands, can be classified as geometrically unstable if the fine particles are smaller than the pore sizes [15,16]. Regarding gap-graded soils, evidence from earthquake-induced liquefaction failure case histories has indicated that they are often involved in liquefaction failures. The fines content (FC) is the most important index for characterizing the particle size distribution of gap-graded soils [17,18]. With reference to these materials, studies by Iwasaki and Tatsuoka [19], Salgado et al. [20], Chien and Oh [21], Choo and Burns [22] and Wichtmann et al. [23] have shown a decrease in G_{max} as FC increases, and this reduction can be reflected in the fitting parameters of G_{max} expression by extending Equation (1). On the other hand, Goudarzy et al. [24], Ruan et al. [25] and Akhyani and Ghalandarzadeh [26] observed that the G_{max} decreases to a minimum at a certain FC, after which it increases with further increases in FC. At a low fines content, the soil behavior is governed by the coarse fraction ("coarse-dominated"), whereas beyond a threshold fines content, it becomes governed by the fines ("fines-dominated"). This threshold marks the transition from a "fines-in-coarse" to a "coarse-in-fines" skeletal structure [27]. Additionally, the influence of FC on the G_{max} can also be explained through the concept of equivalent granular void ratio (e^*) proposed by Thevanayagam et al. [28]. Furthermore, a substantial body of research indicates that particle shape plays a critical role in determining the maximum shear modulus of soils. Particle shape is usually characterized by sphericity (S), roundness (R), aspect ratio (AR) and other shape descriptors [29,30]. However, there remains controversy regarding the influence of particle shape. For instance, Qian et al. [31] found that the maximum shear modulus of angular sands is larger than that of sub-rounded sands. However, Cho et al. [32] compiled a database of natural and crushed sands from the literature and concluded that an increase in the particle irregularity of sand grains leads to a decrease in stiffness. Subsequently, some researchers argued that, to isolate the effect of particle shape, it is essential to exclude other confounding factors. Consequently, they recommended conducting comparisons under conditions of identical particle size distributions. Under these conditions, based on bender element tests, Pham et al. [33] and Liu and Yang [34] found that greater particle

irregularity corresponds to a higher maximum shear modulus. Recently, several scholars have explored the use of advanced 3D printing technology to more effectively isolate the influence of particle shape from other confounding factors, thereby advancing geotechnical testing methodologies. Nevertheless, the findings obtained through this approach remain inconclusive; for instance, Ahmed and Martinez [35] reported an increase in G_{max} with increasing particle roundness, sphericity, and regularity. However, Liang et al. [36] demonstrated that irregular particle morphology markedly increases the G_{max} of uniformly graded sand. This suggests that the observed discrepancies may stem, in part, from the challenges in quantitatively characterizing particle shapes, which often necessitate the use of multiple indices, and, in part, from the experimental control conditions employed. The Discrete Element Method (DEM) simulations offer an effective approach to mitigate the experimental challenges and limitations associated with natural granular materials. DEM investigations using clumped particles to model irregular granular shapes have shown that greater particle irregularity enhances shear stiffness at very small strains [37,38].

Despite significant progress in investigating the relationship among particle shape, particle gradation, and the maximum shear modulus, two key issues remain unresolved. First, most studies examining the influence of particle shape on the maximum shear modulus have predominantly focused on materials with uniform or continuous gradation, while the effects on materials with discontinuous gradation remain insufficiently explored. Second, research that concurrently considers the effects of fines content and variations in particle shape on the maximum shear modulus is scarce. Consequently, it remains unclear whether the relationship between maximum shear modulus and particle shape is influenced by particle gradation, and vice versa. In natural conditions, soil types often differ simultaneously in multiple aspects, such as particle gradation and particle shape. Although sampling from the original soil mass allows for the determination of soil parameters, it is difficult to decouple the combined effects of various physical properties on mechanical behavior. Therefore, quantifying the individual contribution of a single property to the mechanical response of soils remains challenging. To address these gaps, this study employs the DEM to strictly control all variables. By conducting numerical simulations on samples with varying fine particle content and particle shapes, the study aims to elucidate the mechanisms and trends of these two factors on the maximum shear modulus at both macroscopic and microscopic levels. Furthermore, based on the Hardin model, an in-depth discussion is provided on the correlation between particle shape, gradation parameters, and empirical coefficients. Note that all simulated soils herein are non-cohesive, and the fine particles are non-plastic fines that do not strictly adhere to the <0.075 mm criterion commonly adopted in geotechnical engineering or soil classification standards [39]. Therefore, the mechanical property changes arising from clay plasticity effects are not considered.

2. Numerical Simulation Approach

The commercially available DEM software PFC^{3D} (5.0.35) [40] was used for this investigation. A binary mixture is a special representation of gap-graded soils. To investigate the effect of fines content on G_{max}, numerical samples were created, including binary mixtures of coarse and fine particles with fines content of 10% and 20%, as well as single-sized samples consisting only of coarse particles with zero fines content. A simplified Hertz–Mindlin contact model was used with particle density set to 2600 kg/m^3, particle shear modulus set to 29.0 GPa and particle Poisson's ratio set to 0.15 with reference to Gu and Yang [41] and Gong et al. [42]. In the Hertz–Mindlin model, the normal contact force has the following nonlinear relationship with the normal overlap:

$$F_n = \frac{4}{3} E^* \sqrt{R^*} \delta_n^{3/2} \quad (4)$$

where E^* is the equivalent Young's modulus, R^* stands for the equivalent particle radius, δ_n represents the normal overlap between particles.

The normal stiffness is expressed as

$$k_n = 2E^* \sqrt{R^* \delta_n} \tag{5}$$

The incremental tangential contact force can be simplified as

$$\Delta F_t = k_t \Delta s \tag{6}$$

where $k_t = 8G^* \sqrt{R^* \delta_n}$, G^* is the equivalent shear modulus and Δs is the incremental tangential contact displacement.

The sizes of coarse and fine particles were 25.0 mm and 4.0 mm, respectively. To examine the effect of particle shape on the G_{max}, five distinct particle shapes were selected for analysis (Figure 1), each corresponding to a distinct group of samples. The particle labels and shape parameters of the five particles are summarized in Table 1. The particle shape was quantified using the regularity (ρ) proposed by Cho et al. [32], defined as the arithmetic mean of sphericity S and roundness R: $\rho = (S + R)/2$. Roundness is the ratio of the average radius of the surface features to the radius of the largest sphere inscribed in the sand particle, and sphericity is the ratio of the radius of the largest inscribed sphere in the particle to the smallest circumscribed sphere to the particle. In general, particles with ρ close to 1.0 are nearly spherical. Most natural sand particles have regularity values between 0.6 and 1.0, covering the most common subrounded and subangular particle morphologies in engineering soils [43]. All particle models with different shapes established in this study are designed within this reasonable range. This approach provides a consistent and quantitative measure of particle shape across all samples. The sphericity and roundness of a given particle were determined as follows [44]:

$$S = \frac{r_{\text{max-in}}}{r_{\text{max-cir}}} \tag{7}$$

$$R = \frac{\sum r_i / N}{r_{\text{max-in}}} \tag{8}$$

where $r_{\text{max-in}}$ and $r_{\text{min-cir}}$ are the diameters of the largest inscribed and smallest circumscribed spheres and $\Sigma r_i / N$ is the average radius of the particle corners.

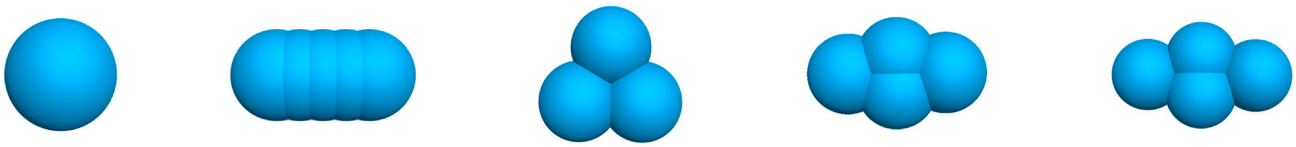

(**a**) (**b**) (**c**) (**d**) (**e**)

Figure 1. Schematic of five selected particles. (**a**) A; (**b**) B; (**c**) C; (**d**) D; (**e**) E.

Table 1. Description parameters for the particle shapes.

Particle Label	Sphericity (S)	Roundness (R)	Regularity (ρ)
A	1.00	1.00	1.00
B	0.50	1.00	0.75
C	0.57	0.93	0.75
D	0.57	0.80	0.69
E	0.50	0.80	0.65

The particles were initially placed randomly in non-contacting positions within a cube modeled using six rigid walls. The samples were generated as follows. Particles were generated with the inter-particle friction coefficient μ set to zero. Then, the sample was subjected to a confining stress of 10 kPa and cycled until reaching equilibrium, with four inter-particle friction coefficients of 0.001, 0.05, 0.1, and 0.3 used to generate samples of different void ratios. Samples with μ = 0.001 produced the densest packing, whereas those with μ = 0.3 resulted in the loosest packing. After this initial preparation, the inter-particle friction coefficient was set to a fixed value of μ = 0.5 for the subsequent isotropic consolidation phase. The system was then subjected to five different stress states (100, 300, 500, 700, and 900 kPa) by servo control of the walls. Triaxial compression simulations with a constant confining pressure and small increments in axial strain were then carried out to determine the G_{max} of granular materials. Figure 2 shows a flow chart of the entire simulation process.

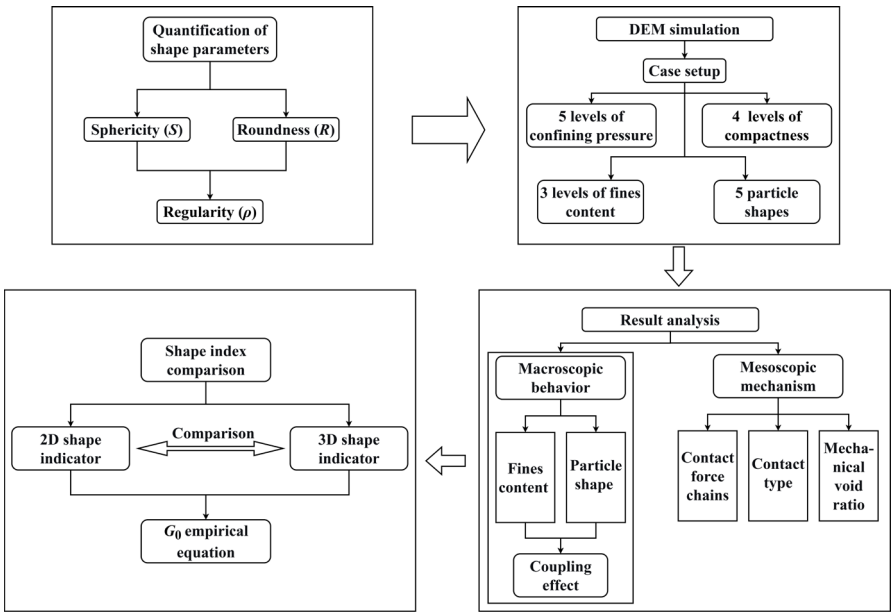

Figure 2. DEM numerical simulation flow chart.

The small increments in axial strain were applied by servo control at an extremely low loading strain rate of 10^{-7} imposed on the top and bottom walls to shear the granular sample under fully quasi-static conditions. During shearing, the positions of the other four side walls are adjusted in real time based on the numerical stress servo control scheme to keep the confining pressure p' constant, and the unbalanced force ratio of the system remains strictly lower than 10^{-5} throughout the whole shearing process until the shear strain γ reached 10^{-6}, so that the sample response could be considered isotropic and elastic. G_{max} was calculated using $G_{max} = \Delta\sigma_1/2\Delta\gamma$, where $\Delta\sigma_1$ represents the axial stress increment. A total of 300 simulation tests were conducted for five different particle shapes at three fines contents, four void ratios, and five confining pressures. Prior to the test, a series of simulations was performed under rigid boundary confinement to determine the initial specimen size L. Specifically, the initial side lengths of three specimens were tentatively set to 200 mm, 220 mm, and 240 mm for confining pressures of 100 kPa and 300 kPa, respectively. The inter-particle friction coefficient was set to 0.3 to generate relatively loose specimens. Figure 3 presents the relationship between axial stress increment $\Delta\sigma_1$ and axial strain increment $\Delta\varepsilon_1$. The results indicate that the specimen size has no discernible effect on the stress–strain response when the ratio of initial side length to maximum particle size ranges between 8 and 9.6. As the influence of boundary conditions is not the focus of this

study, the initial specimen size was ultimately set to 220 mm for computational efficiency. This choice yields a specimen size-to-maximum particle size ratio of 8.8, exceeding the value recommended by Gu et al. [41] to avoid potential size or scale effects.

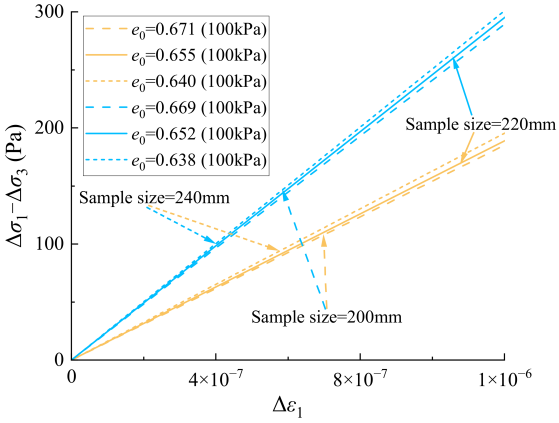

Figure 3. Sensitivity analysis of sample size.

Three typical granular mixtures of *FC* = 20% are shown in Figure 4. Sample labels sequentially refer to particle label, initial void ratio before shearing (e_0), and initial confining pressure. For example, B_0.422_100 denotes a sample composed of particle B with e_0 = 0.422 and an initial confining pressure of 100 kPa.

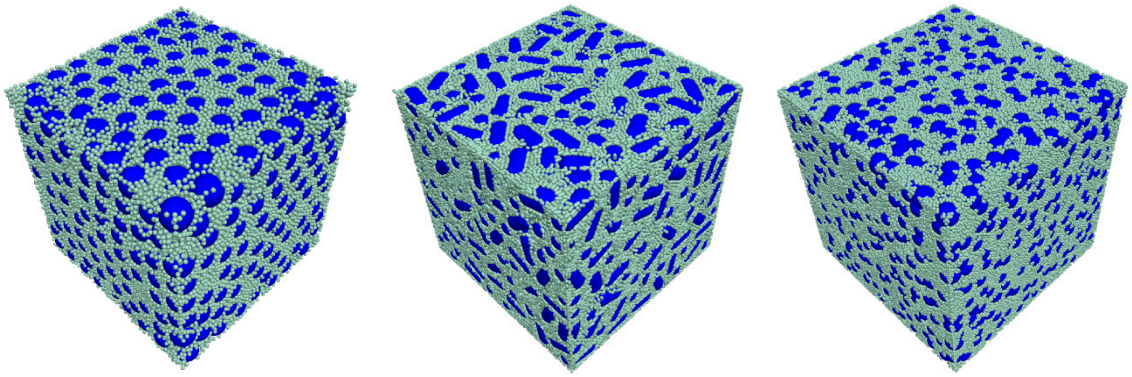

Figure 4. Typical granular mixtures of *FC* = 20%. (**a**) Particle shape A; (**b**) Particle shape B; (**c**) Particle shape C.

3. Results and Discussion

3.1. Macroscopic Properties

Figure 5 presents G_{max} as a function of p' at *FC* = 10% for samples with different initial void ratios. It can be observed that, irrespective of initial compactness, G_{max} increases markedly with p', exhibiting a clear power–law relationship. To further verify the reliability of the numerical simulation results in this study, the experimental results for round glass beads [45] and Ottawa sand [34] are also plotted in the same figure. The comparison shows that the trends of these experimental results are in good agreement with those of the simulated results in this study. Figure 6 shows the dependence of G_{max} on e for the two shapes (p' = 100 kPa). The results indicate that, at a given confining pressure, G_{max} decreases monotonically with increasing e. Moreover, increasing *FC* shifts the G_{max}–e curves to the left, suggesting that, for a given p' and e, higher fines content reduces G_{max}. Similar trends were observed for the other particle shapes and confining pressures; for brevity, these results are not shown separately. The above findings align with the results of previous laboratory experiments and DEM simulations [46–48].

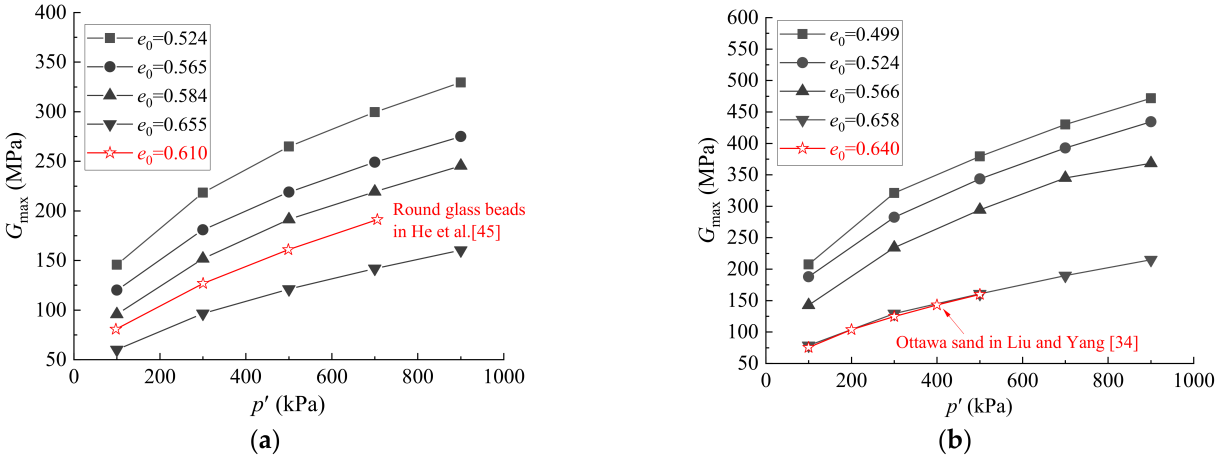

Figure 5. Variation of G_{max} with p' for samples with FC = 10%. (**a**) Particle shape A; (**b**) Particle shape B.

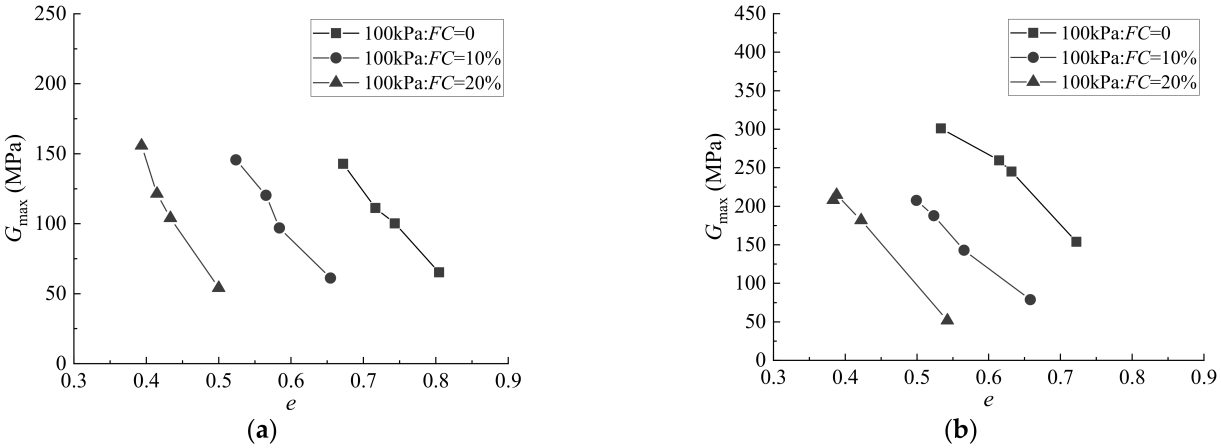

Figure 6. Variation of G_{max} with e for samples with different fines content. (**a**) Particle shape A; (**b**) Particle shape B.

Figure 7 presents the comparison of the G_{max}–e relationships for samples with five particle shapes, with confining pressure held constant at p' = 100 kPa. It is evident from the figure that the G_{max}–e curves for all non-spherical particles lie above that of spherical particles. Notably, the sample with the lowest particle regularity ρ = 0.65 (i.e., the most irregular particle shape) exhibits the highest G_{max}. This observation suggests that, under otherwise similar conditions, G_{max} generally increases as particle shape regularity decreases. From the perspective of physical mechanism, irregular particles possess more surface edges and corners and stronger interparticle interlocking effects, which can form a particle skeleton structure with higher stability and stiffness. Under small-strain loading conditions, such structural characteristics effectively restrain the slight sliding and rotation of particles, thereby greatly improving the overall shear stiffness of granular materials. In contrast, spherical particles have smooth contact surfaces and tend to slide easily relative to each other, leading to weak interlocking constraints and consequently a lower overall value of G_{max}. Further analysis of the results under varying fines content reveals that, as FC increases, the dispersion of the G_{max}–e curves for the three particle shapes (B, C and D) expands significantly. Specifically, when FC = 0, the differences in G_{max} among different particle shapes are relatively minimal; however, as FC increases to 10% and 20%, the disparities in G_{max} between samples with different shapes become more pronounced. Under constant void ratio conditions at FC of 0, 10%, and 20%, the most irregularly shaped particle samples exhibit an increase in G_{max} of approximately 40–120%, 80–152%, and 90–245%, respectively, relative to ideal spherical particles. This increase is less pronounced at lower void ratios.

This behavior indicates that the influence of particle shape on G_{max} is dependent on the fines content, suggesting a coupled effect between FC and ρ in determining G_{max}. Furthermore, for samples in groups B and C, which share the same regularity ρ, their moduli are comparable only at FC = 0. In contrast, for samples in groups C and D, which have different regularity indices, their moduli remain relatively similar across all three levels of FC. The above results indicate that the void ratio e alone cannot fully account for the effects of fines content and particle shape on the maximum shear modulus.

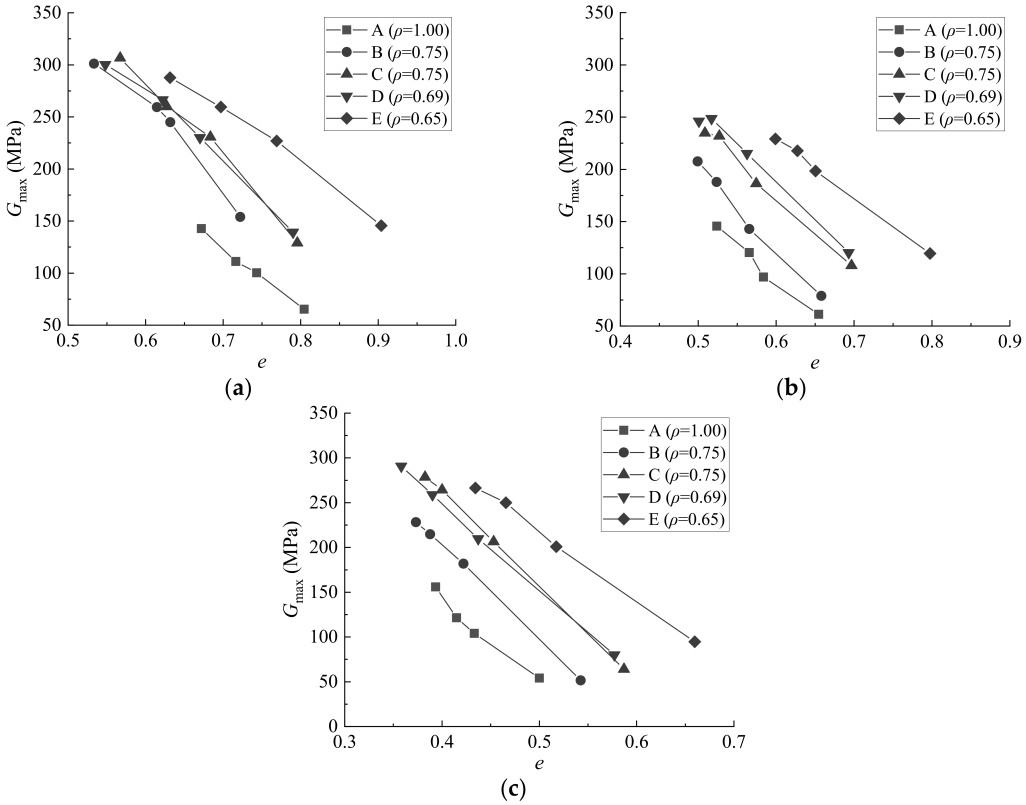

Figure 7. Variation of G_{max} with e for samples with different particle shapes under p' = 100 kPa. (**a**) FC = 0; (**b**) FC =10%; (**c**) FC = 20%.

3.2. Micromechanical Interpretations

The empirical G_{max}–e relationships in Figures 6 and 7 exhibit significant scatter, suggesting that the conventional Hardin model in Equation (1) cannot be directly applied to reliably predict the maximum shear modulus of soils with different fine contents and particle shapes. This limitation highlights the need to identify more representative state variables, particularly at the microscale, to better characterize and predict G_{max}. The coordination number (CN) is a widely used microscopic index for granular materials. Following Thornton [49], CN is calculated as $CN = (2C - N_1)/(N - N_0 - N_1)$, where C is the total number of contacts, N is the number of particles, N_0 represents the number of particles without any contact, and N_1 refers to the number of particles with only one contact. Furthermore, Otsubo [50] proposed a mechanical void ratio, e_m, which only considers active particles, and is calculated as

$$e_m = \frac{V_v + V_{ina}}{V_a} \tag{9}$$

where V_v is the volume of voids, V_{ina} is the volume of rattlers, and V_a is the volume of the remaining active particles.

Figure 8 illustrates the relationships between e_m and G_{max} for particle shapes A and B at p' = 100 kPa. The data reveal that the G_{max}–e_m relationship remains largely insensitive to

variations in *FC*, suggesting that e_m effectively normalizes the impact of different fines contents on the maximum shear modulus. These findings are consistent with the observations of Zhu et al. [51] and support the role of the coordination number as a microscopic state variable governing the G_{max} in soils with varying particle size distributions.

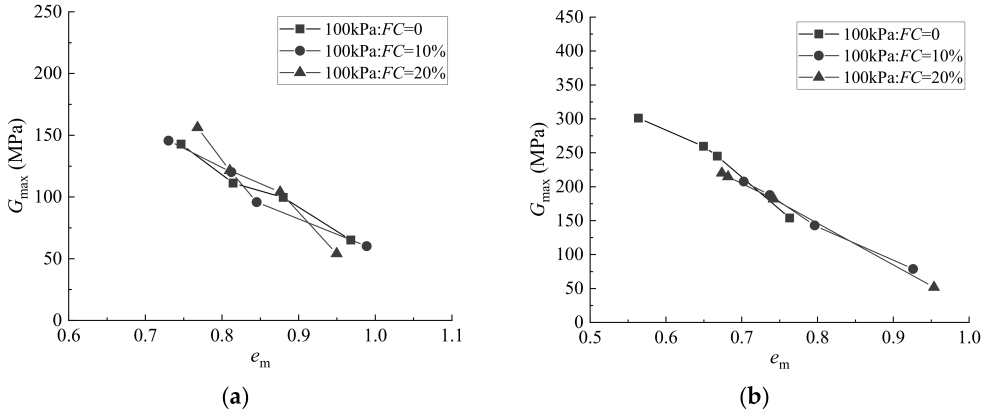

Figure 8. Variation of G_{max} with e_m for samples with different fines content. (**a**) Particle shape A; (**b**) Particle shape B.

Figure 9 presents a comparison of the G_{max}–e_m relationships across five different particle shapes. While a general trend is discernible, the G_{max}–e_m curves exhibit significant scatter, suggesting that the mechanical void ratio e_m is insufficient to fully capture the variations in stiffness arising from particle shape. These findings align with those of Hu et al. [52] and Zhou and Xu [53], demonstrating that relying solely on the coordination number is insufficient to eliminate the effect of particle shapes. Therefore, to achieve a more comprehensive understanding, it is necessary to quantify the relationship between e_m and e under different fines content and particle shapes. This approach is expected to improve the interpretation of the G_{max} and enhance the predictive capability of models that incorporate both microstructural and macroscopic parameters.

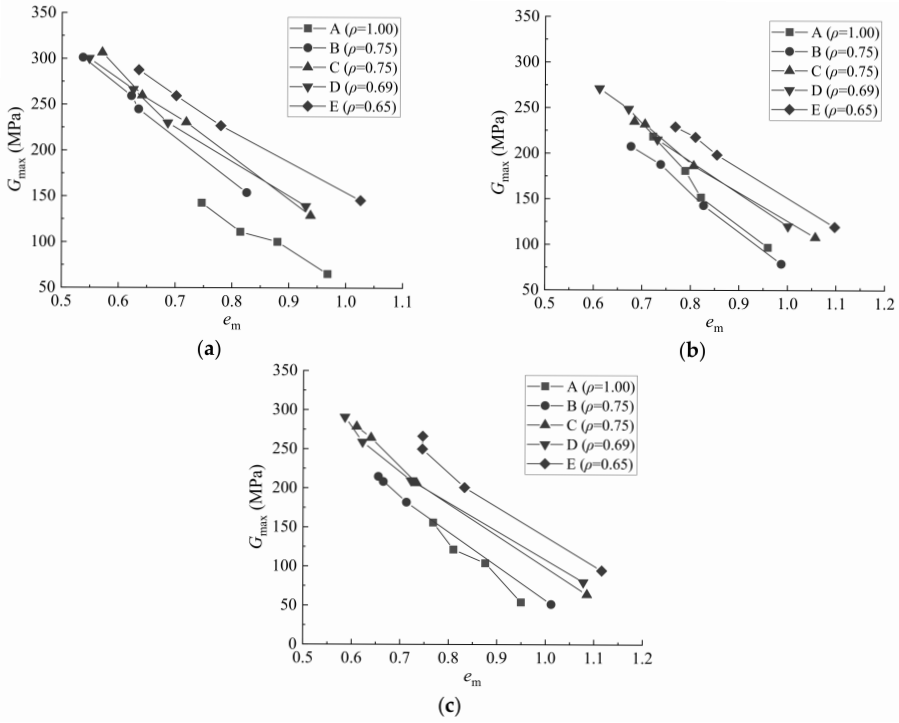

Figure 9. Variation of G_{max} with e_m for samples with different particle shapes under p' = 100 kPa. (**a**) *FC* = 0; (**b**) *FC* = 10%; (**c**) *FC* = 20%.

Figure 10a shows the variation of the e_m/e ratio with *FC* for five different particle shapes. The results indicate that the relationship can be closely described by a linear function in Equation (10). At a given void ratio, e_m/e increases with *FC*, suggesting that the reduction in G_{max} is primarily due to an increased proportion of inactive particles, leading to an increase in e_m. Figure 10b shows the variation of the e_m/e ratio with the particle shape regularity factor ρ for three distinct fines content. The data reveal that the relationship between e_m/e and ρ is significantly influenced by *FC*. Although e_m/e vs. ρ exhibits some scatter, e_m/e generally decreases with decreasing ρ (i.e., increasing particle irregularity), particularly at *FC* = 20%. These findings suggest that, for a given *FC*, the number of rattlers with zero or one contact diminishes as particle shape irregularity increases. The above results explain the greater scatter observed in Figure 9 compared with Figure 8.

$$\frac{e_m}{e} = aFC + b \tag{10}$$

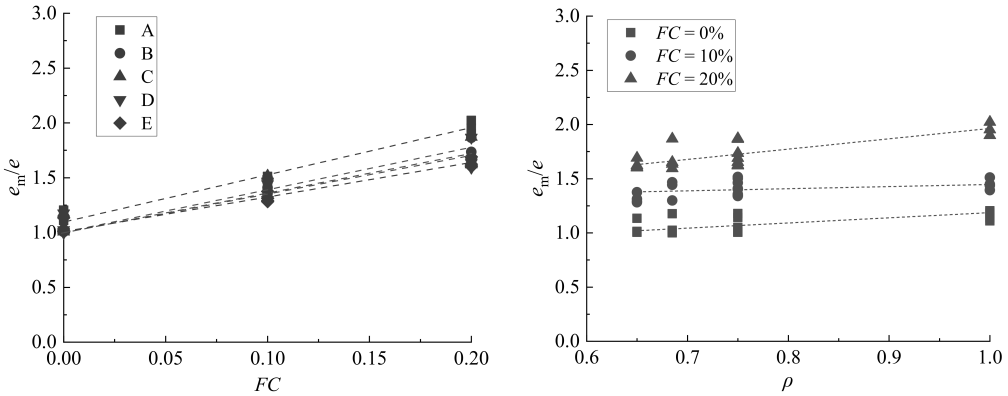

(**a**) e_m/e vs. *FC* (**b**) e_m/e vs. ρ

Figure 10. Variation of e_m/e with (**a**) *FC* and (**b**) ρ.

To more effectively illustrate the impact of particle shape and fines content on G_{max}, particle contacts are categorized into three distinct types: "coarse–coarse (c-c)" contact, "coarse–fine (c-f)" contact, and "fine–fine (f-f)" contact. Figure 11 presents the three-dimensional representation of the contact type for five samples with different particle shapes, with similar initial void ratios (the corresponding e_0 values for shape A to shape E are 0.433, 0.422, 0.453, 0.437, and 0.459 for 20% fines content, and 0.584, 0.566, 0.575, 0.563, and 0.599 for 10% fines content) and a confining pressure of 100 kPa. Similarly, Figure 12 illustrates the contact type for particle shape C across different fines content, with corresponding e_0 values of 0.567, 0.575, and 0.587 for fines content of 0, 10%, and 20%, respectively. As shown in Figure 11, with an increase in fines content, the number of coarse–fine and fine–fine contacts rises significantly. Compared to samples composed of spherical particles, those with irregular particle shapes exhibit a more pronounced increase in the number of fine–fine and coarse–fine contacts, while the variation in coarse–coarse contacts remains relatively limited across these samples. Furthermore, the number of coarse–coarse decreases significantly with an increase in the fines content, as shown in Figure 12. Figures 11 and 12 also provide an explanation for the observed smaller scatter of e_m/e values in samples with different particle shapes at a constant fines content (Figure 10a), compared to the larger scatter observed in samples with the same particle shape but varying fines content (Figure 10b).

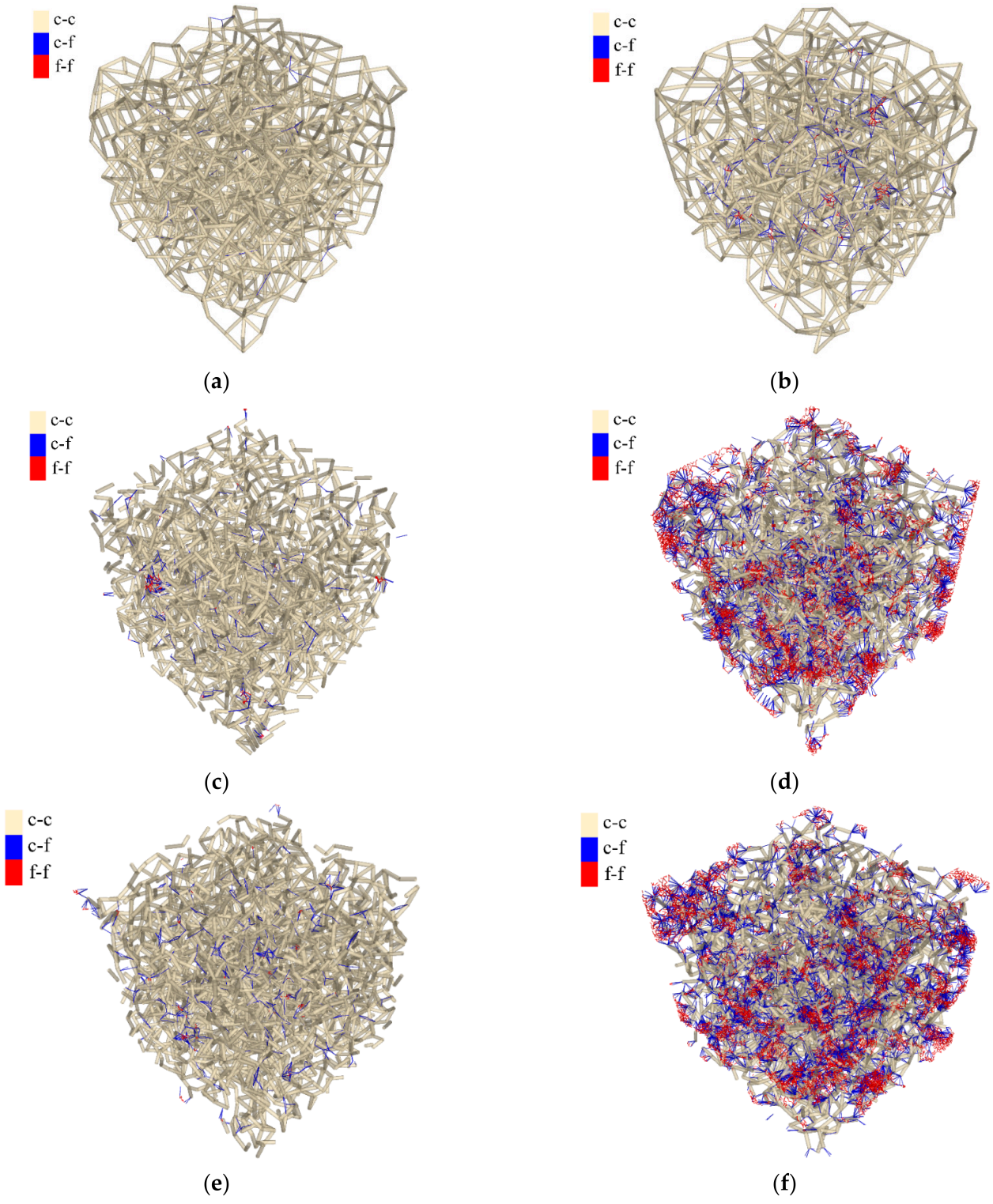

Figure 11. *Cont.*

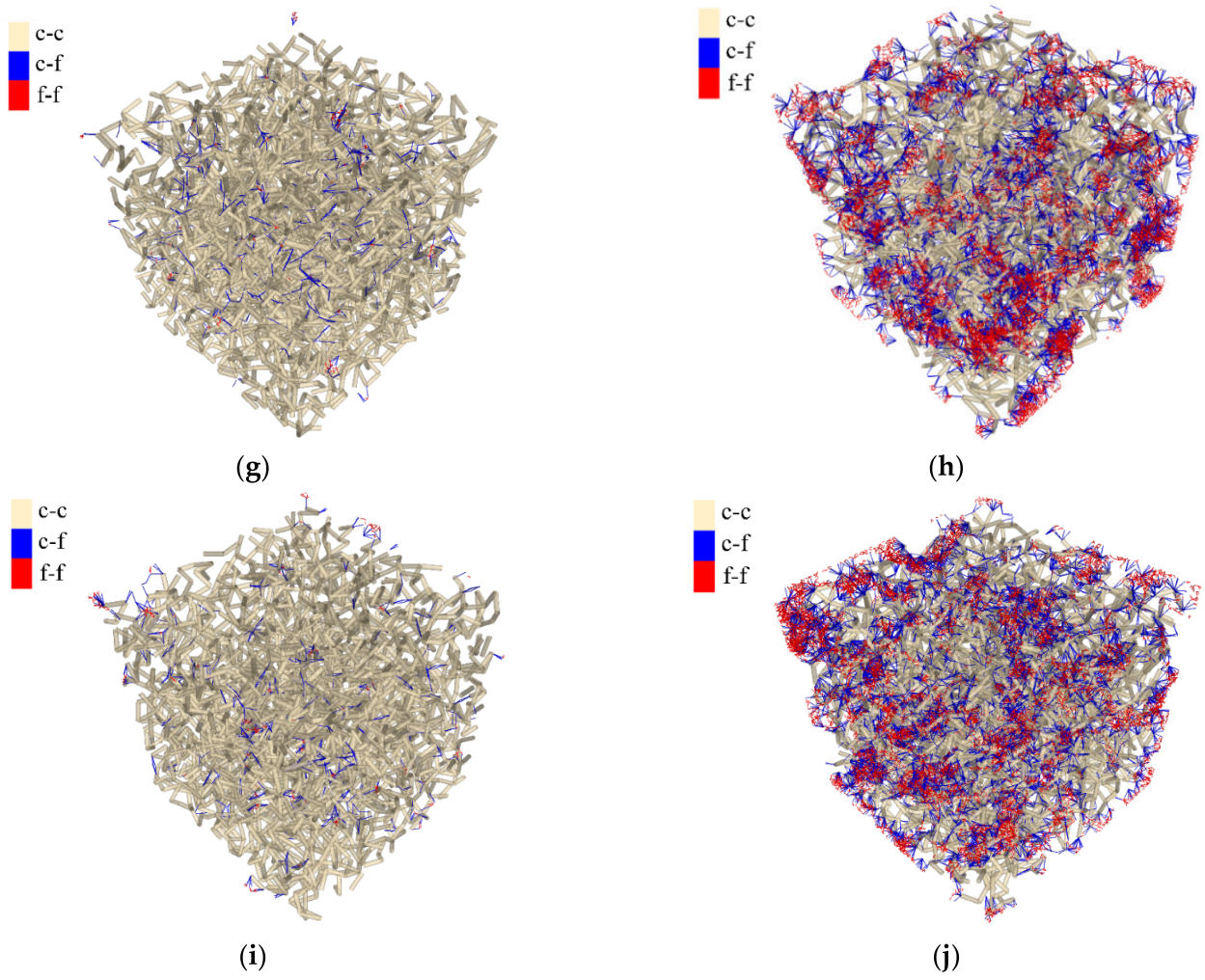

Figure 11. Three-dimensional representation of the normal contact force network for samples with different particle shapes. (**a**) Shape A (*FC* = 10%); (**b**) Shape A (*FC* = 20%); (**c**) Shape B (*FC* = 10%); (**d**) Shape B (*FC* = 20%); (**e**) Shape C (*FC* = 10%); (**f**) Shape C (*FC* = 20%); (**g**) Shape D (*FC* = 10%); (**h**) Shape D (*FC* = 20%); (**i**) Shape E (*FC* = 10%); (**j**) Shape E (*FC* = 20%).

Based on the coordination number (*CN*), the partial coordination numbers corresponding to the three types of contacts, namely "coarse–coarse" (CN_{cc}), "coarse–fine" (CN_{cf}), and "fine–fine" (CN_{ff}), can be defined respectively as follows:

$$CN_{cc} = \frac{2C_{cc} - N_1}{N_c + N_f - N_0 - N_1} \tag{11}$$

$$CN_{cf} = \frac{2C_{cf} - N_1}{N_c + N_f - N_0 - N_1} \tag{12}$$

$$CN_{ff} = \frac{2C_{ff} - N_1}{N_c + N_f - N_0 - N_1} \tag{13}$$

where C_{cc} is the number of coarse–coarse contacts; C_{cf} is the number of coarse–fine contacts; C_{ff} is the number of fine–fine contacts; N_c is the number of coarse particles; N_f is the number of fine particles.

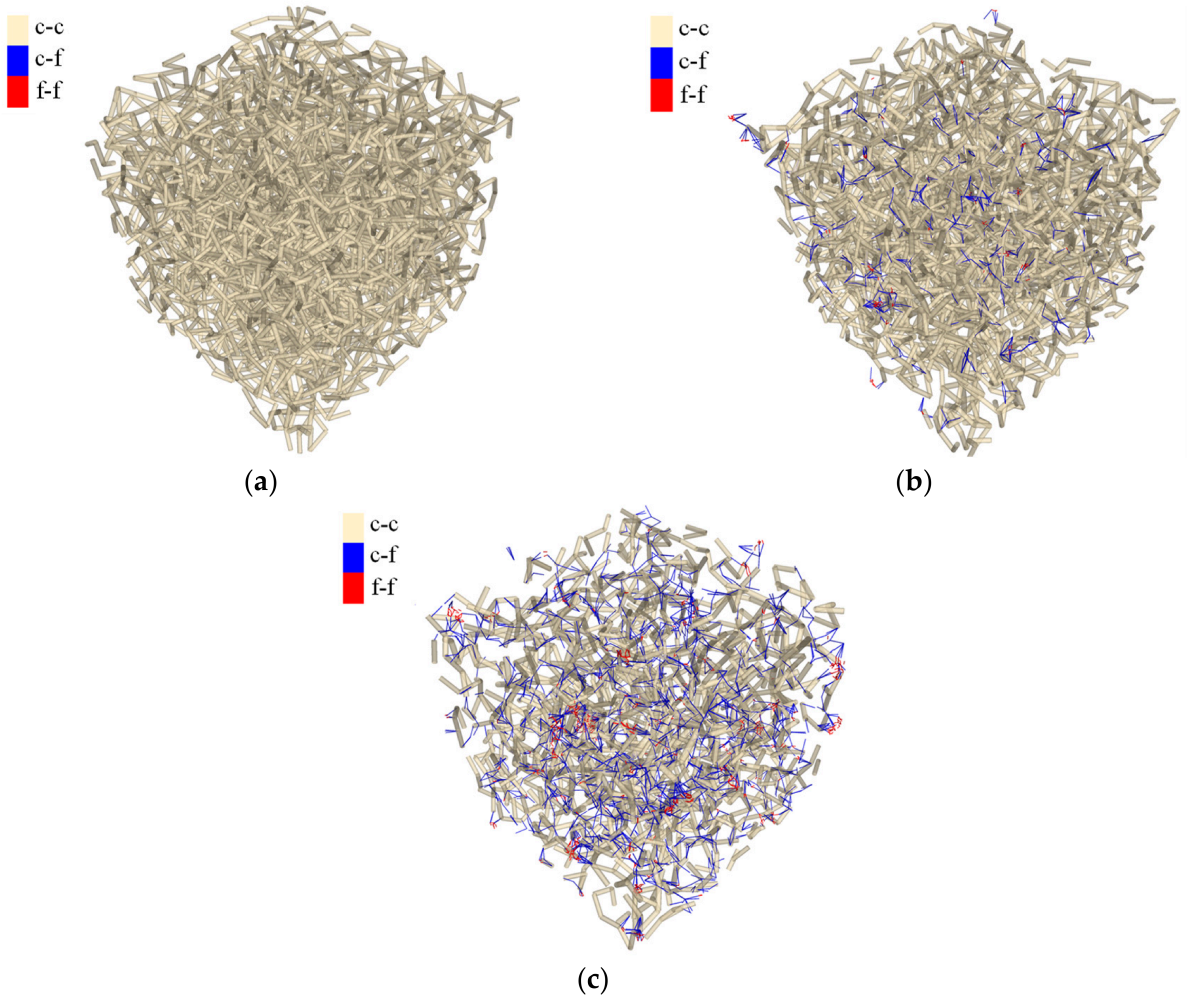

Figure 12. Three-dimensional representation of the normal contact force network for samples with different fines content. (**a**) Shape C (*FC* = 0); (**b**) Shape C (*FC* = 10%); (**c**) Shape C (*FC* = 20%).

Figure 13 presents the variations of CN_{cc}/CN, CN_{cf}/CN, and CN_{ff}/CN with *FC* for five samples with different particle shapes under the loosest and densest states. The results show that as *FC* increases, CN_{cc}/CN gradually decreases, while CN_{cf}/CN and CN_{ff}/CN gradually increase, which is consistent with the previous findings. Moreover, for samples with more irregular shapes, the decrease in CN_{cc}/CN is more pronounced, whereas the increases in CN_{cf}/CN and CN_{ff}/CN are smaller. This indicates that irregularly shaped coarse particles originally exhibit strong interlocking and occlusion effects, but the addition of fine particles more easily disrupts the original coarse particle skeleton, leading to a rapid decline in the coarse–coarse contact number. Meanwhile, due to the complex geometry of irregular particles, it is difficult for fine particles to form numerous stable new contacts with coarse particles, so the increases in the coarse–fine and fine–fine contact ratios are limited. Comparing the densest and loosest states, it can be observed that the variations of the three contact ratios with *FC* are more significant in the densest state, indicating that in the densest state, the inter-particle contacts of irregularly shaped samples are more susceptible to interference from *FC*. In contrast, in the loosest state, the particle arrangement is relatively loose, and the addition of fine particles has a relatively minor effect on the original contact structure.

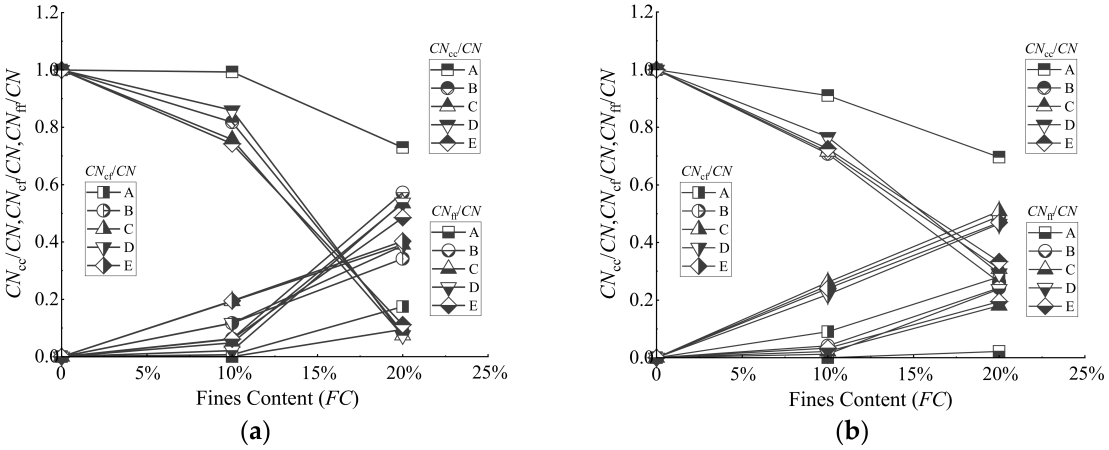

Figure 13. Variation of CN_{cc}/CN, CN_{cf}/CN and CN_{ff}/CN with *FC*. (**a**) Densest state; (**b**) Loosest state.

3.3. Empirical Model of G_{max} Considering FC and ρ

Since e_m alone does not fully capture particle shape effect, separate G_{max} models were developed for each particle shape based on Equation (1). This approach allows for a more comprehensive representation of the shape-dependent variations in the mechanical properties of granular materials. Incorporating the relationship between e_m/e and *FC*, Equation (1) can be presented as Equation (14). The unknown coefficients *A*, *a*, *b*, *c*, and *n* in the model are determined through the least-square method using the simulation data.

$$G_{max} = A((aFC + b)e)^c \left(\frac{p'}{p_a}\right)^n \tag{14}$$

Table 2 presents the corresponding fitting parameters of Equation (14) for samples with different particle shapes. Figure 14 shows the relationships between these model parameters and particle shape regularity *ρ*. The results indicate that the three parameters *A*, *a*, and *c* exhibit clear and systematic trends with particle shape, suggesting that they are strongly influenced by particle shape. In contrast, the remaining two model parameters show minimal variation across different shapes, indicating a lesser sensitivity to shape effects. The limited variation in *n* indicates that the Hertz–Mindlin contact model is applicable solely to the interactions between smooth, elastic particles. It fails to account for the influence of surface roughness on the contact behavior between two particles [54,55]. These findings provide quantitative insights into the influence of particle shape on the mechanical response of granular assemblies and identify the parameters most indicative of shape effects.

Table 2. Least-square fitting parameters of Equation (14).

Group	*A*	*c*	*n*	*a*	*b*	R^2
A	57.88	−3.33	0.32	3.99	1.12	0.91
B	75.25	−2.56	0.34	3.51	1.05	0.93
C	105.60	−2.13	0.34	3.14	1.07	0.93
D	112.92	−1.82	0.34	3.18	1.05	0.92
E	138.85	−1.84	0.34	2.96	1.03	0.92

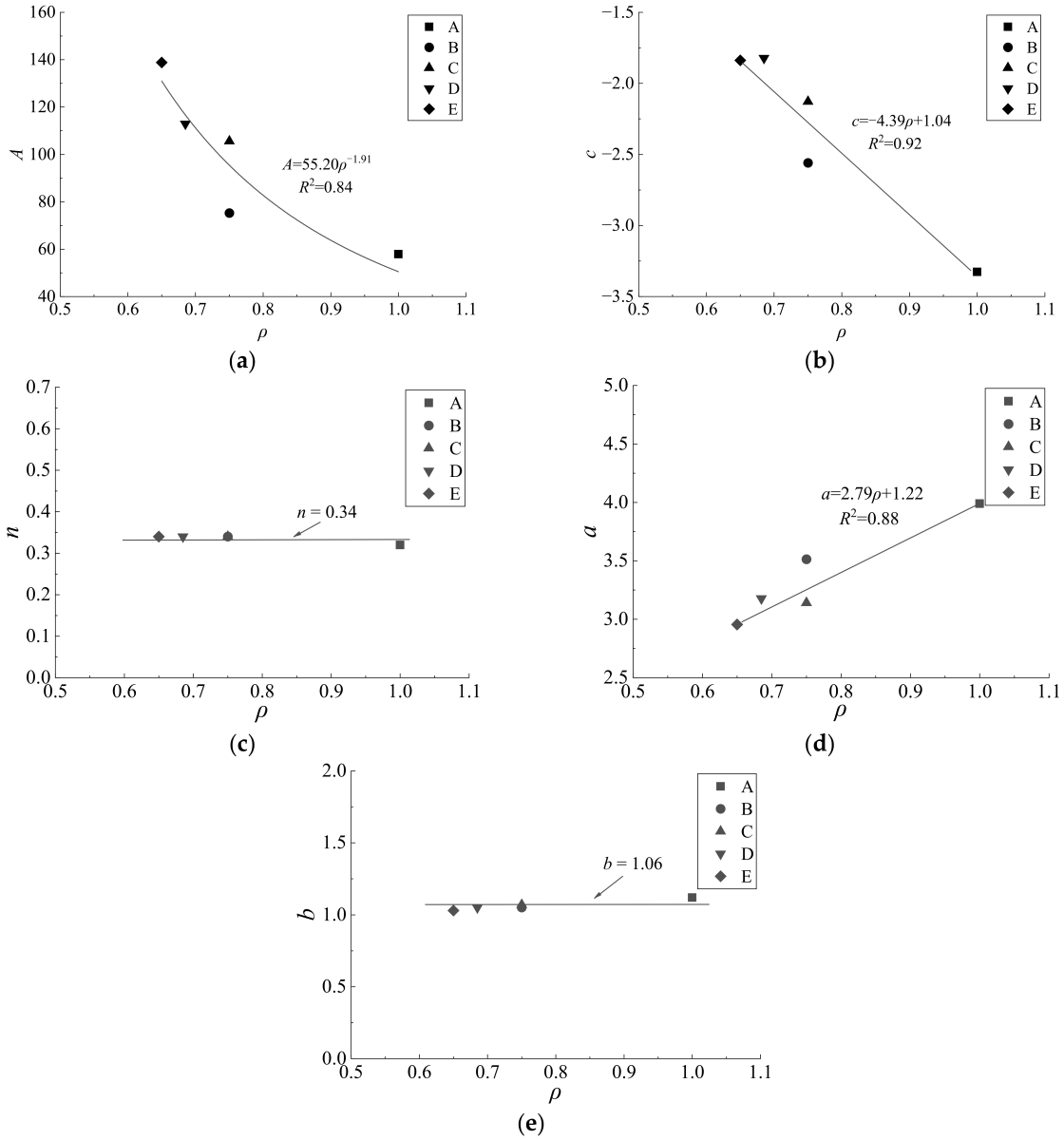

Figure 14. Dependence of model parameters on particle shape index. (**a**) A vs. ρ; (**b**) c vs. ρ; (**c**) n vs. ρ; (**d**) a vs. ρ; (**e**) b vs. ρ.

Based on the relationships between the model parameters and the regularity ρ presented in Figure 14, a G_{max} prediction model that incorporates the effects of fines content, particle shape, void ratio, and confining pressure was derived, as shown in Equation (15). Figure 15 compares the predicted and actual G_{max} values, demonstrating that the overall predictive performance of this model is satisfactory. The majority of the measured data points across the five particle shapes fall within the ±20% error band, with the coefficient of determination (R^2) reaching 0.90.

$$\begin{cases} G_{max} = A((aFC + b)e)^c (p'/p_a)^n \\ A = 55.20\rho^{-1.91} \\ c = -4.39\rho + 1.04 \\ n = 0.34 \\ a = 2.79\rho + 1.22 \\ b = 1.06 \end{cases} \quad (15)$$

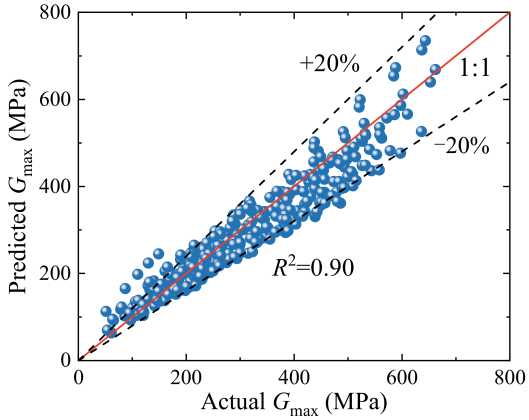

Figure 15. Actual and predicted G_{max} values by Equation (9).

3.4. Improvement of Empirical Model of G_{max} Considering 3D Shape Index

In this study, two of the simulated conditions exhibit distinctive particle shapes, namely Group B and Group C. Specifically, the sphericity *S* and the roundness *R* for Group B are 0.50 and 1.00, whereas those for Group C are 0.57 and 0.93. Despite identical ρ, the model parameters *A*, *a*, and *c* differ significantly (Figure 14). To investigate the underlying causes of this discrepancy, Figure 16 compares the number of contacts between coarse–coarse, coarse–fine, and fine–fine contacts for two samples under nearly identical void ratios at *FC* = 0%, 10% and 20%. It is observed that the sample with *S* = 0.57 and *R* = 0.93 is consistently higher than that for the sample with *S* of 0.50 and *R* of 1.00, particularly at *FC* = 20%, resulting in a higher overall G_{max} for the former (as seen in Figure 7). These findings indicate that using a two-dimensional regularity index as a comprehensive metric for particle shape has inherent limitations.

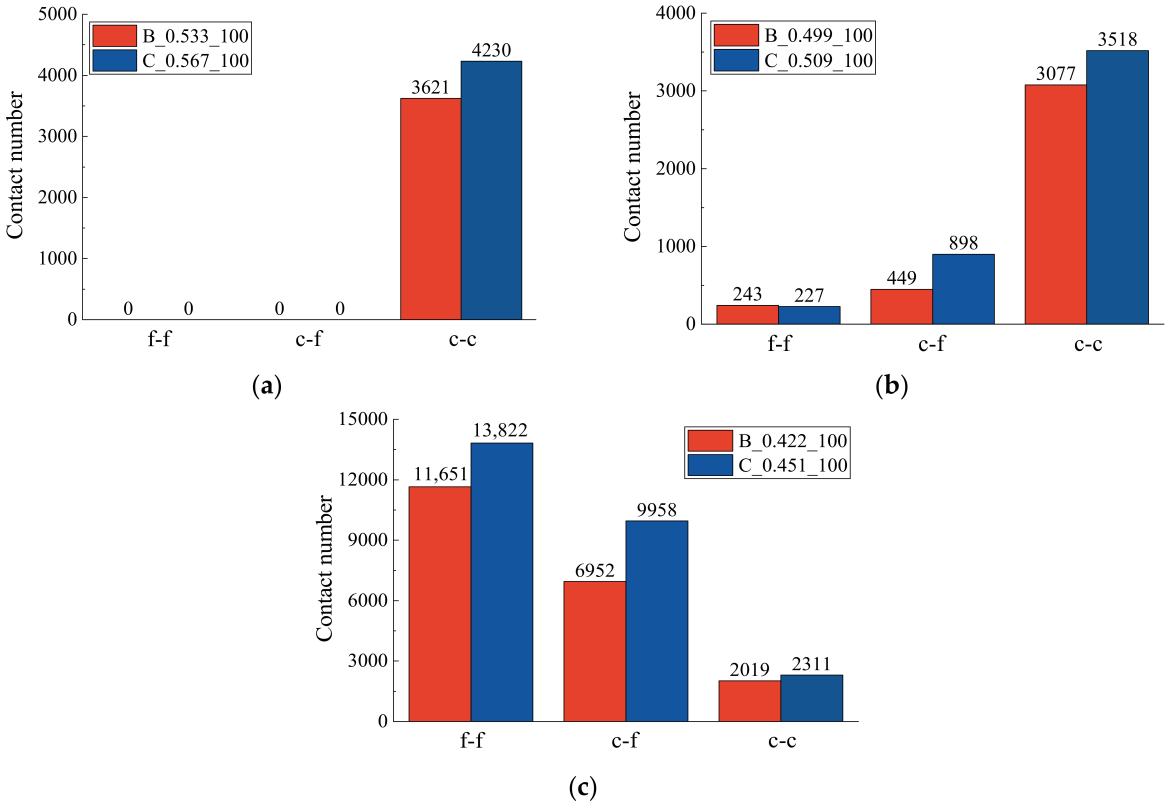

Figure 16. Number of three different types of contact. (**a**) *FC* = 0; (**b**) *FC* = 10%; (**c**) *FC* = 20%.

Two-dimensional shape indices, primarily derived from two-dimensional projections, provide only a limited representation of particle regularity and are inadequate for fully capturing the spatial morphological characteristics of particles, particularly for concave structures [56,57]. Recent advancements in three-dimensional image analysis enable the computation of sphericity and roundness based on particle geometry. Drawing on the quantitative evaluation methods for three-dimensional shape descriptors proposed by Nie et al. [37], this study computed the three-dimensional sphericity (S^{3D}) and roundness (R^{3D}) of five different particle types. From these calculations, the three-dimensional regularity (ρ^{3D}) was derived using a stereoscopic approach. ρ^{3D} of a given particle was determined as follows:

$$\rho^{3D} = \frac{S^{3D} + R^{3D}}{2} \tag{16}$$

$$S^{3D} = \frac{\sqrt[3]{36\pi V^2}}{A_s} \tag{17}$$

$$R^{3D} = \frac{\frac{1}{N}\sum_{i=1}^{N} r_i}{r_{\max,\mathrm{ins}}} \tag{18}$$

where V and A_s are particle volume and surface area, $r_{\max,\mathrm{ins}}$ is the maximum inscribed sphere radius.

The results of 2D and 3D shape descriptors are presented in Table 3. As shown, the 3D regularity indicators of shapes B and C, which exhibit identical 2D regularity, differ, with shape C being more irregular. Figure 17 shows that ρ^{3D} exhibits a more consistent correlation with the model parameters A, a, and c, particularly for shapes B and C, indicating an improved characterization of particle shape effects.

Table 3. Comparison between 2D and 3D particle shape descriptors.

Group	S^{2D}	R^{2D}	ρ^{2D}	S^{3D}	R^{3D}	ρ^{3D}
A	1.00	1.00	1.00	1.00	1.00	1.00
B	0.50	1.00	0.75	0.91	1.00	0.96
C	0.57	0.93	0.75	0.84	0.93	0.88
D	0.57	0.80	0.69	0.87	0.80	0.83
E	0.50	0.80	0.65	0.80	0.80	0.80

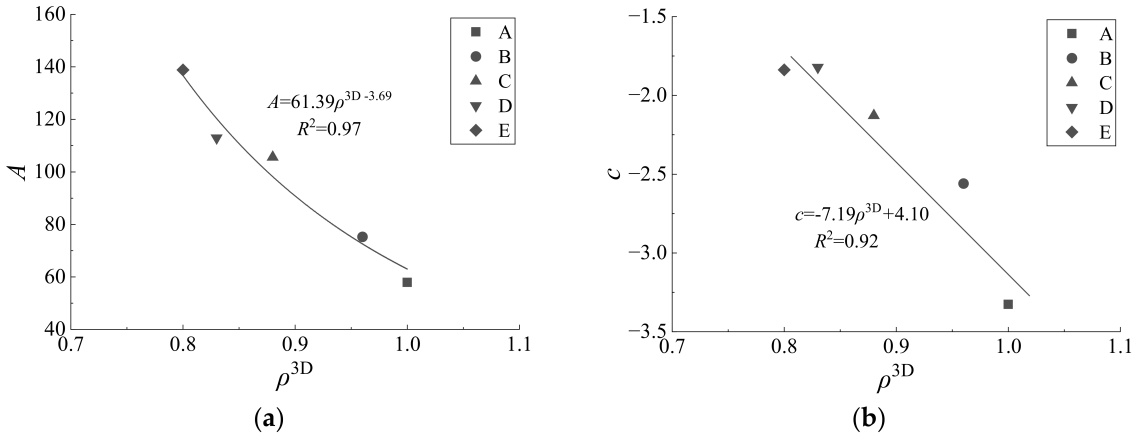

Figure 17. *Cont.*

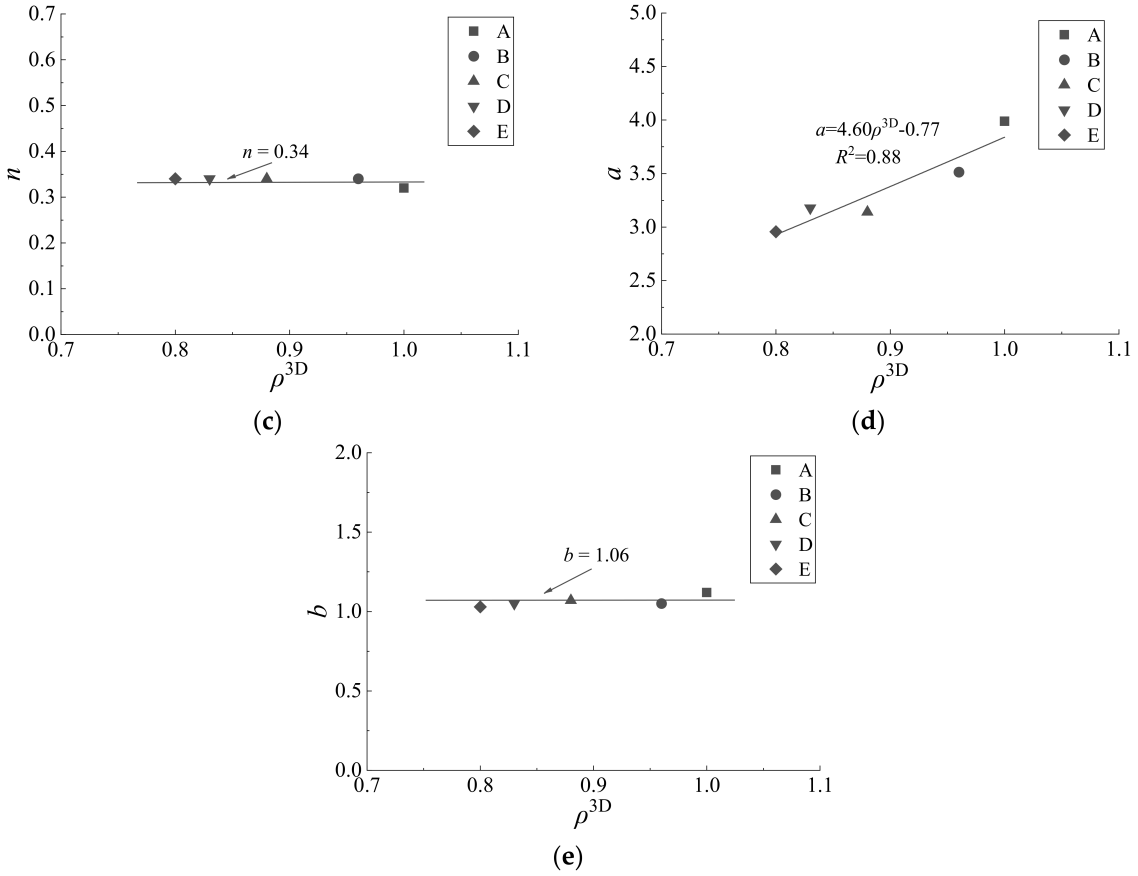

Figure 17. Dependence of model parameters on 3D particle shape index. (**a**) A vs. ρ^{3D}; (**b**) c vs. ρ^{3D}; (**c**) n vs. ρ; (**d**) a vs. ρ; (**e**) b vs. ρ.

A prediction model of G_{max} based on ρ^{3D} was developed using the same methodology, as described in Equation (19). Figure 18 presents a comparison between the G_{max} values predicted by Equation (19) and the observed values, demonstrating enhanced performance relative to Equation (15) with the coefficient of determination R^2 of 0.94. This improvement indicates that ρ^{3D} more accurately captures the influence of particle shape on the maximum shear modulus. Therefore, when two-dimensional shape indices are identical, three-dimensional shape parameters should be prioritized in the analysis. These results highlight the importance of considering the full three-dimensional geometry of particles when assessing their mechanical properties in granular media.

$$\begin{cases} G_{max} = A((aFC + b)e)^c (p'/p_a)^n \\ A = 61.39\left(\rho^{3D}\right)^{-3.69} \\ c = -7.19\rho^{3D} + 4.10 \\ n = 0.34 \\ a = 4.60\rho^{3D} - 0.77 \\ b = 1.06 \end{cases} \quad (19)$$

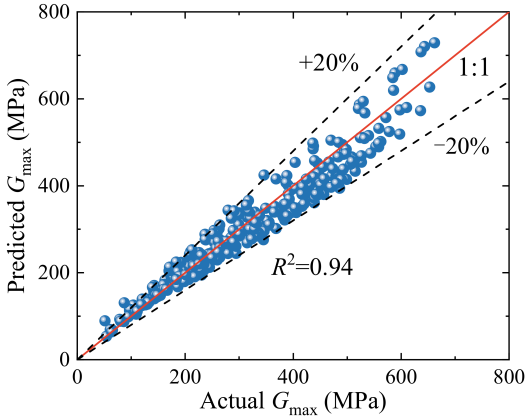

Figure 18. Actual and predicted G_{max} values by Equation (13).

4. Limitation of the Present Study and Future Work

Although this study demonstrated the coupled effects of fines content and particle shape on the G_{max} of gap-graded granular mixtures using a knowledge-driven approach, several limitations should be acknowledged. First, the maximum non-plastic fines content was restricted to 20%, which is below the threshold fines content. It is recommended that simulations over a wider range of PSD be conducted to investigate whether and when the relationship between G_{max} and particle characteristic parameters changes with further increasing *FC* to a certain value. Doing so would allow the construction of a complete response curve, clarify the link between skeleton evolution and modulus variation, and thereby enhance the comprehensiveness and academic rigor of the conclusions. Second, all simulations were performed under isotropic consolidation conditions, without considering the influence of stress anisotropy—which is prevalent in actual engineering contexts—on G_{max}. This leads to a gap between the findings and real-world engineering scenarios. It is advisable to include comparative analyses under different stress ratios, to discuss the coupled effects of stress anisotropy, particle shape, and fines content. Such an extension would broaden the applicability of the research and increase its engineering value. Finally, the Hertz–Mindlin model cannot account for particle surface roughness and real contact characteristics (e.g., early-stage plastic deformation, tangential nonlinearity), and the results are sensitive to model parameters. Further validation with laboratory tests is needed in future work.

5. Conclusions

This study systematically investigated the coupled effects of fines content and particle shape on the maximum shear modulus of gap-graded granular materials using the discrete element method. Based on the numerical results and micromechanical analyses, the following conclusions can be drawn:

(1) G_{max} increases with mean effective stress p' and decreases with void ratio e. At the same p' and e (i.e., other conditions being consistent), an increase in *FC* reduces G_{max}; specifically, when *FC* increases from 0 to 20%, G_{max} can decrease by 30–80%. Meanwhile, a decrease in particle regularity (i.e., more irregular shapes) obviously increases G_{max}; under the same other conditions, the G_{max} of the sample with the most irregular particle shape can be increased by approximately 40–245% compared with that of ideal spherical particles. In addition, a significant coupled effect exists, where the influence of particle shape on G_{max} becomes more pronounced as *FC* increases.

(2) The mechanical void ratio e_m, which excludes inactive particles, effectively normalizes the effect of *FC* on G_{max}, resulting in a unique $G_{max}-e_m$ relationship for each particle

shape. However, e_m does not fully eliminate the influence of particle shape, as the $G_{max}-e_m$ curves still show notable dispersion across different particle shapes. This residual effect is attributed to variations in the proportion of inactive particles, with more irregular shapes exhibiting fewer rattlers and thus higher stiffness.

(3) By incorporating the relationship between e_m/e and FC, an extended Hardin-type model was developed to predict G_{max} as a function of e, p', FC, and ρ. The model parameters A, a, and c show clear correlations with particle shape, while the stress exponent n remains relatively constant due to the use of the Hertz–Mindlin contact model.

(4) In contrast to the two-dimensional regularity index ρ^{2D}, the three-dimensional regularity index ρ^{3D} provides a more accurate representation of particle morphology, resulting in a refined prediction model with enhanced accuracy (R^2 = 0.94), as compared to the model using ρ^{2D} (R^2 = 0.90). This highlights the critical role of three-dimensional shape parameters in accurately characterizing the mechanical behavior of granular soils.

(5) From the perspective of particle packing and contact mechanics, when the fines content does not exceed 10%, coarse–coarse contacts remain absolutely dominant, irrespective of particle shape. At a fines content of 20%, for assemblies composed of spherical particles, coarse–coarse contacts still predominate. In contrast, for mixtures containing irregularly shaped particles, the number of coarse–fine and fine–fine contacts increases significantly. These findings not only offer practical guidance for the judicious selection of filler materials in engineering applications but also suggest that the proposed approach—integrating particle-scale characteristics into engineering-scale models—can enhance the predictive robustness of geotechnical practice.

This study has several limitations. First, only non-plastic fines below the threshold ($\leq$20%) were considered, restricting generalizability to soils containing plastic fines. Second, isotropic consolidation was assumed, neglecting common stress anisotropy. Third, the Hertz–Mindlin contact model cannot represent surface roughness or realistic contact characteristics. Future work should extend validation to wider PSD ranges and stress ratios, and adopt more sophisticated contact models.

Author Contributions: Conceptualization, X.W.; methodology, Y.T.; software, X.A.; validation, X.A.; formal analysis, X.W.; investigation, Y.T.; resources, X.L.; data curation, X.A.; writing—original draft preparation, Y.T., X.W., X.A. and X.L.; writing—review and editing, X.W. and X.L.; visualization, X.L.; supervision, X.W.; project administration, X.L.; funding acquisition, X.L. All authors have read and agreed to the published version of the manuscript.

Funding: This research was funded by National Natural Science Foundation of China (Grant number 52309173); Fund of National Dam Safety Research Center (Grant number CX2023B01); Open Research Fund of Key Laboratory of Reservoir and Dam Safety Ministry of Water Resources (Grant number YK324010), and Open Research Fund of Key Laboratory of Construction and Safety of Water Engineering of the Ministry of Water Resources, China Institute of Water Resources and Hydropower Research (Grant Number: IWHR-ENGI-202501).

Data Availability Statement: The datasets for this study are available from the corresponding author upon reasonable request.

Conflicts of Interest: The authors declare no conflicts of interest.

Abbreviations

The following abbreviations are used in this manuscript:

AR	Aspect Ratio
CN	Coordination number
DEM	Discrete Element Method
e	Void Ratio

e_0	Initial Void Ratio
e^*	Equivalent Granular Void Ratio
e_m	Mechanical Void Ratio
FC	Fines Content
G_{max}	Maximum Shear Modulus
HSS	Hardening Soil Small Strain
p'	Mean Effective Stress
R	Roundness
R^2	Coefficient of Determination
R^{3D}	Three-dimensional Roundness
S	Sphericity
S^{3D}	Three-dimensional Sphericity
ρ	Regularity
ρ^{3D}	Three-dimensional Regularity

References

1. Suliman, M.; Khan, M.; Islam, Z.U. Enhancing Predictive Accuracy and Interpretability of Small Strain Shear Modulus for Granular Soils Using Machine Learning Models. *Transp. Infrastruct. Geotechnol.* **2026**, *13*, 42. [CrossRef]
2. Wang, Y.; Shi, Y.; Yang, T.Y.; Wang, W.; Sun, Z.; Zhang, Y. Structural performance warning based on computer intelligent monitoring and fractional-order multi-rate kalman fusion method. *Fractal Fract.* **2026**, *10*, 186.
3. Krause, V.; Goudarzy, M.; Wichtmann, T. Volumetric Shear Strain Threshold and Maximum Shear Modulus: Data Analysis and Resonant Column Experiments. *Int. J. Geomech.* **2026**, *26*, 04026011. [CrossRef]
4. Zhao, C.; Pei, B.G.; Zeng, G.H.; Lu, G.; Ju, Y. Determination of key parameters for the small-strain hardening soil model and engineering validation: A case study of typical soils in Taiyuan, China. *Buildings* **2026**, *16*, 922. [CrossRef]
5. Zheng, X.; Wang, X.W.; Shen, K.M.; Gu, X. Determination of HSS model parameters for soft clays in Hangzhou: Statistical analysis and engineering validation. *Buildings* **2025**, *15*, 3886. [CrossRef]
6. Basas, V.G.; Pantazopoulos, I.A.; Atmatzidis, D.K. Torsional and flexural resonant column testing of grouted sands. *Soil Dyn. Earthq. Eng.* **2020**, *139*, 106360. [CrossRef]
7. Parsa, M.; Bagheripour, M.H.; Lo Presti, D.C.F. Experimental and Simulation Study on Dynamic Properties of Two Historical Soils in Italy. *Int. J. Civ. Eng.* **2023**, *21*, 887–904.
8. Morsy, A.M.; Salem, M.A.; Elmamlouk, H.H. Evaluation of dynamic properties of calcareous sands in Egypt at small and medium shear strain ranges. *Soil Dyn. Earthq. Eng.* **2019**, *116*, 692–708. [CrossRef]
9. Jovîčić, V.; Coop, M. *Stiffness of Coarse-Grained Soils at Small Strains*; Emerald Publishing: Leeds, UK, 1998.
10. Le, C.M.; Sarkar, D.; Koenig, D.; Goudarzy, M.; Wichtmann, T. Small and Intermediate Strain Characteristics of a Partially Saturated Sand-Clay Mixture. *Int. J. Geomech.* **2023**, *23*, 04023115. [CrossRef]
11. Chen, Y.; Yang, J. Small-Strain Shear Modulus of Quartz Sands under Anisotropic Stress Conditions. *J. Geotech. Geoenviron. Eng.* **2024**, *150*, 04024033. [CrossRef]
12. He, S.H.; Goudarzy, M.; Ding, Z.; Sun, Y.; Xu, T.; Zhang, Q.-F. Small-strain shear modulus (Gmax) and microscopic pore structure of calcareous sand with different grain size distributions. *Granul. Matter* **2022**, *24*, 112. [CrossRef]
13. Wei, X.; Zhang, T.; Yang, Z.X.; Yang, J. The effects of particle size and surface roughness on the small-strain shear modulus of sands. *Geotechnique* **2025**, *75*, 1594–1607. [CrossRef]
14. Hardin, B.O.; Black, W.L. Sand Stiffness Under Various Triaxial Stresses. *J. Soil Mech. Found. Div.* **1966**, *92*, 27–42. [CrossRef]
15. Jamiolkowski, M.; Lancellotta, R.; Presti, D.L. Remarks on the stiffness at small strains of six Italian clays. In *Developments in Deep Foundations and Ground Improvement Schemes*; CRC Press: Boca Raton, FL, USA, 1995; pp. 197–216.
16. Mehdizadeh, A.; Disfani, M.M.; Evans, R.; Arulrajah, A.; Ong, D.E.L. Mechanical Consequences of Suffusion on Undrained Behaviour of a Gap-Graded Cohesionless Soil—An Experimental Approach. *Geotech. Test. J.* **2017**, *40*, GTJ20160145. [CrossRef]
17. Kokusho, T. Liquefaction strengths of poorly graded and well-graded granular soils investigated by lab tests. In *Proceedings of the Earthquake Geotechnical Engineering: 4th International Conference on Earthquake Geotechnical Engineering-Invited Lectures, Thessaloniki, Greece, 25–28 June 2007*; Springer: Dordrecht, The Netherlands, 2007; pp. 159–184.
18. Manzanal, D.; Bertelli, S.; Lopez-Querol, S.; Rossetto, T.; Mira, P. Influence of fines content on liquefaction from a critical state framework: The christchurch earthquake case study. *Bull. Eng. Geol. Environ.* **2021**, *80*, 4871–4889. [CrossRef]
19. Iwasaki, T.; Tatsuoka, F. Effects of grain size and grading on dynamic shear moduli of sands. *Soils Found.* **1977**, *17*, 19–35. [CrossRef]

20. Salgado, R.; Bandini, P.; Karim, A. Shear strength and stiffness of silty sand. *J. Geotech. Geoenviron. Eng.* **2000**, *126*, 451–462. [CrossRef]
21. Chien, L.K.; Oh, Y.N. Influence of fines content and initial shear stress on dynamic properties of hydraulic reclaimed soil. *Can. Geotech. J.* **2002**, *39*, 242–253. [CrossRef]
22. Choo, H.; Burns, S.E. Shear wave velocity of granular mixtures of silica particles as a function of finer fraction, size ratios and void ratios. *Granul. Matter* **2015**, *17*, 567–578. [CrossRef]
23. Wichtmann, T.; Navarrete Hernandez, M.A.; Triantafyllidis, T. On the influence of a non-cohesive fines content on small strain stiffness, modulus degradation and damping of quartz sand. *Soil Dyn. Earthq. Eng.* **2015**, *69*, 103–114. [CrossRef]
24. Goudarzy, M.; Koenig, D.; Schanz, T. Small strain stiffness of granular materials containing fines. *Soils Found.* **2016**, *56*, 756–764. [CrossRef]
25. Ruan, B.; Miao, Y.; Cheng, K.; Yao, E.-L. Study on the small strain shear modulus of saturated sand-fines mixtures by bender element test. *Eur. J. Environ. Civ. Eng.* **2021**, *25*, 28–38.
26. Akhyani, S.; Ghalandarzadeh, A. Effect of fines content and particle diameter ratio on maximum shear modulus of dense binary packing of spherical particles. *Granul. Matter* **2022**, *24*, 67. [CrossRef]
27. Zuo, L.; Baudet, B.A. Determination of the transitional fines content of sand-non plastic fines mixtures. *Soils Found.* **2015**, *55*, 213–219. [CrossRef]
28. Thevanayagam, S. Intergrain contact density indices for granular mixes-I: Framework. *Earthq. Eng. Eng. Vib.* **2007**, *6*, 123–134. [CrossRef]
29. Sarkar, D.; Goudarzy, M.; Wichtmann, T. Inspection of various grain morphology parameters based on wave velocity measurements on three different granular materials. *Soil Dyn. Earthq. Eng.* **2022**, *153*, 107071. [CrossRef]
30. Altuhafi, F.N.; Coop, M.R.; Georgiannou, V.N. Effect of Particle Shape on the Mechanical Behavior of Natural Sands. *J. Geotech. Geoenviron. Eng.* **2016**, *142*, 04016071. [CrossRef]
31. Qian, X.; Gray, D.H.; Woods, R.D. Voids and granulometry: Effects on shear modulus of unsaturated sands. *J. Geotech. Eng.* **1993**, *119*, 295–314. [CrossRef]
32. Cho, G.C.; Dodds, J.; Santamarina, J.C. Particle shape effects on packing density, stiffness, and strength: Natural and crushed sands. *J. Geotech. Geoenviron. Eng.* **2006**, *132*, 591–602. [CrossRef]
33. Pham, H.H.G.; Van Impe, P.O.; Van Impe, W.F.; Menge, P.; Haegeman, W. Small-strain shear modulus of calcareous sand and its dependence on particle characteristics and gradation. *Soil Dyn. Earthq. Eng.* **2017**, *100*, 371–379. [CrossRef]
34. Liu, X.; Yang, J. Shear wave velocity in sand: Effect of grain shape. *Geotechnique* **2018**, *68*, 742–748. [CrossRef]
35. Ahmed, S.S.; Martinez, A. Effects of particle shape on the shear wave velocity and shear modulus of 3D printed sand analogs. *Open Geomech.* **2022**, *3*, 1735732. [CrossRef]
36. Liang, H.; Shen, Y.; Chen, S.; Shen, J.; Xu, J. Effect of Multiscale Particle Morphology on Small-Strain Shear Modulus of Irregularly Shaped Sand under Isotropic Consolidation: Triaxial Bender Element Tests on 3D-Printed Sand. *J. Eng. Mech.* **2024**, *150*, 06024001. [CrossRef]
37. Nie, J.Y.; Shi, X.S.; Cui, Y.F.; Yang, Z.-Y. Numerical evaluation of particle shape effect on small strain properties of granular soils. *Eng. Geol.* **2022**, *303*, 106652. [CrossRef]
38. Wu, M.M.; Wu, F.Y.; Wang, J.F. Particle shape effect on the shear banding in DEM-simulated sands. *Granul. Matter* **2022**, *24*, 48. [CrossRef]
39. *D2487-11*; Standard Practice for Classification of Soils for Engineering Purposes (Unified Soil Classification System). ASTM: West Conshohocken, PA, USA, 2006.
40. Itasca. *User's Manual for Pfc3d*; Itasca Consulting Group, Inc.: Minneapolis, MN, USA, 2014.
41. Gu, X.Q.; Yang, J. A discrete element analysis of elastic properties of granular materials. *Granul. Matter* **2013**, *15*, 139–147. [CrossRef]
42. Gong, J.; Wang, X.; Li, L.; Nie, Z. DEM study of the effect of fines content on the small-strain stiffness of gap-graded soils. *Comput. Geotech.* **2019**, *112*, 35–40. [CrossRef]
43. Altuhafi, F.; O'sullivan, C.; Cavarretta, I. Analysis of an image-based method to quantify the size and shape of sand particles. *J. Geotech. Geoenviron. Eng.* **2013**, *139*, 1290–1307. [CrossRef]
44. Payan, M.; Khoshghalb, A.; Senetakis, K.; Khalili, N. Effect of particle shape and validity of Gmax models for sand: A critical review and a new expression. *Comput. Geotech.* **2016**, *72*, 28–41. [CrossRef]
45. He, S.H.; Yin, Z.Y.; Ding, Z.; Li, R.-D. Novel observations for the impact of particle morphology on shear modulus of granular materials. *Acta Geotech.* **2025**, *20*, 4631–4650. [CrossRef]
46. Liu, X.Y.; Zou, D.G.; Liu, J.M.; Zheng, B. Predicting the small strain shear modulus of coarse-grained soils. *Soil Dyn. Earthq. Eng.* **2021**, *141*, 106468. [CrossRef]
47. Liu, X.; Yang, J. Influence of size disparity on small-strain shear modulus of sand-fines mixtures. *Soil Dyn. Earthq. Eng.* **2018**, *115*, 217–224. [CrossRef]

48. Nie, J.Y.; Cui, Y.F.; Wang, G.D.; Wang, R.; Zhang, N.; Zhang, L.; Wu, Z. A comprehensive numerical investigation of multi-scale particle shape effects on small-strain stiffness of sands. *Géotechnique* **2025**, *75*, 323–336. [CrossRef]
49. Thornton, C. Numerical simulations of deviatoric shear deformation of granular media. *Géotechnique* **2000**, *50*, 43–53. [CrossRef]
50. Otsubo, M. Particle Scale Analysis of Soil Stiffness and Elastic Wave Propagation. Doctoral Dissertation, Imperial College, London, UK, 2016.
51. Zhu, Y.; Gong, J.; Nie, Z. Numerical Investigation of the Elastic Properties of Binary Mixtures as a Function of the Size Ratio and Fines Content. *Int. J. Geomech.* **2020**, *20*, 04020155. [CrossRef]
52. Hu, J.; Wu, H.Y.; Gu, X.Q.; Zhou, Q. Particle shape effects on dynamic properties of granular soils: A DEM study. *Comput. Geotech.* **2023**, *161*, 105578. [CrossRef]
53. Zhou, W.X.; Xu, M. DEM analysis of the influence of particle shape on the small-strain stiffness of granular materials. *Comput. Geotech.* **2025**, *179*, 106996. [CrossRef]
54. Sandeep, C.S.; He, H.; Senetakis, K. An experimental micromechanical study of sand grain contacts behavior from different geological environments. *Eng. Geol.* **2018**, *246*, 176–186. [CrossRef]
55. Tsigginos, C.; Zeghal, M. A micromechanical analysis of the effects of particle shape and contact law on the low-strain stiffness of granular soils. *Soil Dyn. Earthq. Eng.* **2019**, *125*, 105693. [CrossRef]
56. Li, L.; Iskander, M. Comparison of 2D and 3D dynamic image analysis for characterization of natural sands. *Eng. Geol.* **2021**, *290*, 106052. [CrossRef]
57. Maroof, M.A.; Mahboubi, A.; Noorzad, A.; Safi, Y. A new approach to particle shape classification of granular materials. *Transp. Geotech.* **2020**, *22*, 100296. [CrossRef]

Disclaimer/Publisher's Note: The statements, opinions and data contained in all publications are solely those of the individual author(s) and contributor(s) and not of MDPI and/or the editor(s). MDPI and/or the editor(s) disclaim responsibility for any injury to people or property resulting from any ideas, methods, instructions or products referred to in the content.